iScience

CellPress
OPEN ACCESS

Article

Tunable Selectivity and High Efficiency of CO_2 Electroreduction via Borate-Enhanced Molten Salt Electrolysis

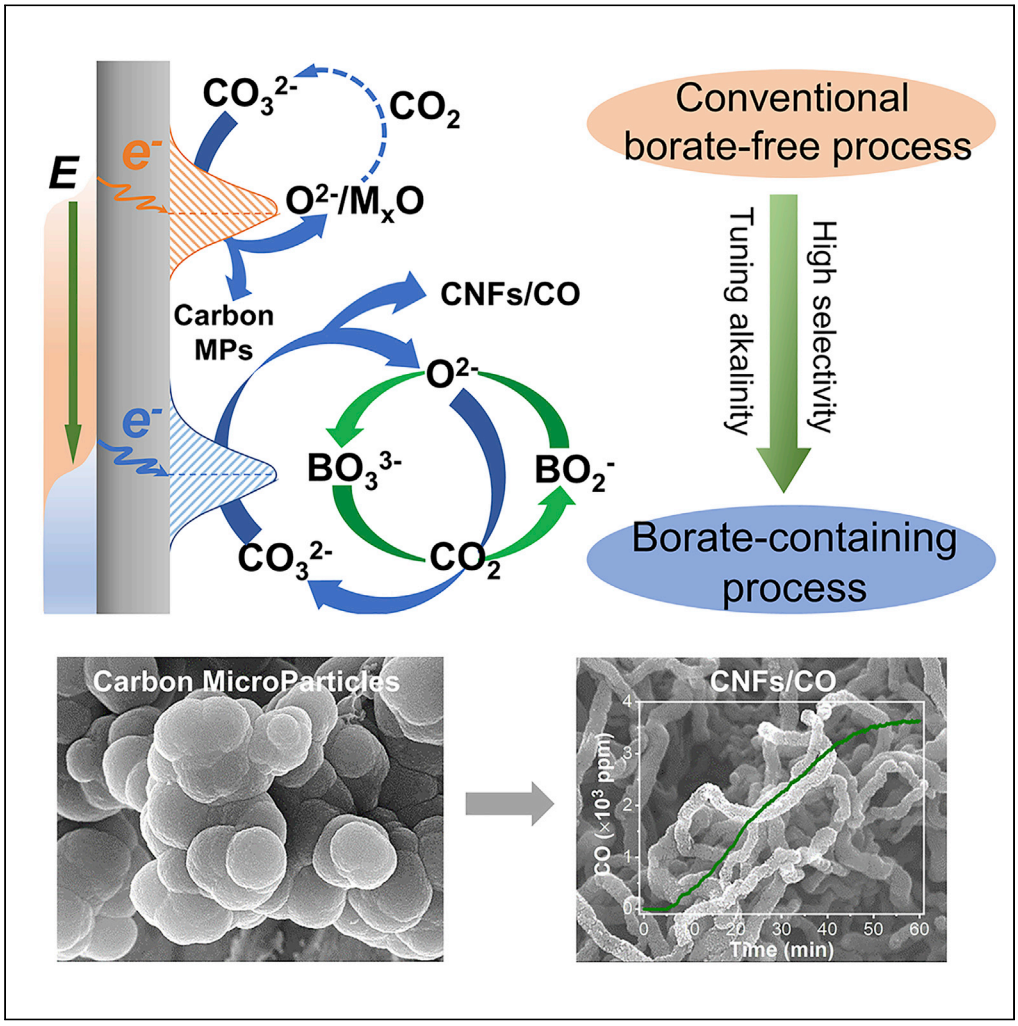

Liangyou Hu, Bowen Deng, Kaifa Du, Rui Jiang, Yanpeng Dou, Dihua Wang

wangdh@whu.edu.cn

HIGHLIGHTS

The product selectivity of CO_2 reduction reaction was highly tunable

Extending product species via regulating electrolyte alkalinity was achieved

Borate-assisted oxygen removal was conducive to produce CO_2-derived CNFs

Lower energy consumption and higher CO_2 conversion efficiency were achieved

Hu et al., iScience *23*, 101607
October 23, 2020
https://doi.org/10.1016/j.isci.2020.101607

iScience

CellPress
OPEN ACCESS

Article

Tunable Selectivity and High Efficiency of CO_2 Electroreduction via Borate-Enhanced Molten Salt Electrolysis

Liangyou Hu,[1,2] Bowen Deng,[1,2] Kaifa Du,[1] Rui Jiang,[1] Yanpeng Dou,[1] and Dihua Wang[1,3,*]

SUMMARY

Converting CO_2 into value-added chemical fuels and functional materials by CO_2 reduction reaction (CO_2RR) is conducive to achieving a carbon-neutral energy cycle. However, it is still challenging to efficiently navigate CO_2RR toward desirable products. Herein, we report a facile strategy to extend product species in borate-containing molten electrolyte at a positively shifted cathodic potential with a high current density (e.g. 100 mA/cm^2), which can selectively electro-transform CO_2 into desired products (either CO or solid carbon nanofibers, respectively reaching a high selectivity of ~90%). The borates can act as a controller of electrolyte alkalinity to buffer the concentration of sequentially generated O^{2-} during CO_2RR, positively shifting the reduction potential of the captured CO_2 and concurrently extending the product species. The sustainable buffering effect is available under CO_2 atmosphere. Compared with borate-free electrolyte, the CO_2 conversion efficiency is over three times higher, while the electrolysis energy consumption is decreased by over 40%.

INTRODUCTION

Ever since the industrial revolution, the atmospheric CO_2 concentration has annually increased due to the anthropogenic emission (He et al., 2013). However, CO_2 can also be regarded as an abundant C_1 feedstock. Converting greenhouse gas CO_2 into value-added chemical fuels and functional materials is both conducive to energy storage and CO_2 mitigation, achieving a carbon-neutral energy cycle (MacDowell et al., 2010). Among various CO_2 reduction reaction (CO_2RR) approaches, electrochemical reduction processes are a simple strategy that can operate under environment-friendly conditions, especially the ones driven by renewable electricity sources (e.g., solar, wind) (Chen et al., 2018; Liu et al., 2019). Great attentions have been paid in various species of electrolytes in recent years, such as room temperature technologies (e.g., aqueous solutions, ionic liquids) (Chen and Mu, 2019; König et al., 2019; Rosen et al., 2011; Zhu et al., 2016), and high-temperature processes (e.g., solid oxide electrolysis cells and molten salt electrolytes) (Jiang et al., 2019; Song et al., 2019; Wu et al., 2018). Considering the fact that linear CO_2 molecule is thermodynamically stable, it is still a great challenge to meet the energy demand for navigating CO_2RR toward desired products more efficiently.

Very recently, due to high selectivity and excellent reaction kinetics, molten salt CO_2 capture and electro-transformation (MSCC–ET) technology has attracted many attentions in converting high-flux CO_2 into value-added products, including CO (Kaplan et al., 2010), carbon nanofibers (CNFs) (Douglas et al., 2017; Licht et al., 2016; Ren et al., 2015), hollow carbon spheres (Deng et al., 2017), ultrathin carbon sheet (Hu et al., 2015), and syngas or hydrocarbons were also achieved in the existence of water vapor (Wu et al., 2016). The high temperature process has some intrinsic advantages over the reduction near room temperature in terms of reaction thermodynamics, kinetics and product selectivity. The temperature of the system can be self-heated by Joule heat originated from the electrolysis process, where no extra energy input is needed to maintain the operating temperature for an industrial cell, making the energy balance more attractive (Sun et al., 2011; Sysoev et al., 2015). In addition, molten salts are also being used as effective media for commercial thermal energy storage heated by concentrated solar power in the world today, a large amount of CO_2 can be reduced if a renewable electricity (e.g., solar, hydroelectric etc.) is applied, with a net CO_2 conversion efficiency of 70–98%, depending on the sources of electricity (Jiang et al., 2019).

[1]School of Resource and Environmental Sciences, Hubei International Scientific and Technological Cooperation Base of Sustainable Resource and Energy, Wuhan University, Wuhan 430072, P. R. China

[2]These authors contributed equally

[3]Lead Contact

*Correspondence: wangdh@whu.edu.cn

https://doi.org/10.1016/j.isci.2020.101607

For conventional MSCC-ET systems, molten carbonates or carbonate-containing halides are the mainstream electrolytes to convert CO_2 into solid carbon/CO, such as Li_2CO_3–Na_2CO_3–K_2CO_3 (Yin et al., 2013), LiCl–NaCl–Na_2CO_3, and $CaCl_2$–$CaCO_3$, etc (Ge et al., 2016b; Ijije et al., 2014a). Among those electrolytes, solid carbon materials are the most preferential CO_2RR products, while electrolysis conditions are critical to gain specific microstructures (Deng et al., 2017, 2018). Although high-yield CO product was only observed in a selected molten electrolyte at a relatively high temperature (>900°C) exclusively using a Ti cathode (Kaplan et al., 2010), it is still challenging to achieve gaseous products under a mild condition due to thermodynamic and kinetic barriers as well as limitations of electrode alternatives (Chery et al., 2014). Moreover, the closed loop of the conventional molten salt CO_2RR process is dependent on the supply of CO_3^{2-} by carbonation of oxygen anions (O^{2-}) with CO_2 (known as acid gas), where the mass transfer of O^{2-} is a rate-determining step (Gao et al., 2018; Deng et al., 2019). However, our recent works revealed that cathodic passivation effect, where solid oxides might easily precipitate on cathode, could favorably occur if the concentration (defined as alkalinity) of generated O^{2-} in the electrolyte was oversaturated (Deng et al., 2019), severely increasing the cathodic polarization and retarding CO_2RR kinetics (Gao et al., 2018). Hence, according to the state of the art, feasible pathways that can regulate product selectivity under mild operating conditions and with enhanced kinetics have not been reported yet.

Herein, we propose a facile strategy to manipulate the CO_2RR selectivity at a positively shifted reduction potential by tuning alkalinity of electrolyte. Taking the conventional molten LiCl–Li_2CO_3 electrolyte for an example, it is demonstrated, for the first time, that adding $LiBO_2$ into the electrolyte can thermodynamically change the reaction pathway compared to that in bare molten LiCl–Li_2CO_3, greatly enhancing CO_2RR kinetics and extending product species at a lower cell voltage. Moreover, a tunable selectivity toward high-yield (~90%) CO_2-derived products (e.g., either CO or CNFs) at a relatively low temperature (e.g. <650°C) was also achieved. It is worth noting that the CO_2 conversion efficiency was improved by over three times in molten LiCl–Li_2CO_3–$LiBO_2$. To the best of our knowledge, the presented $LiBO_2$-containing molten electrolyte is one of the most suitable electrolytes for high-flux CO_2 capture and conversion regarding practical application.

RESULTS AND DISCUSSION

Thermodynamic Characterizations of Alkalinity-Dependent CO_2RR

Taking solid carbon and CO as CO_2RR products for instances, the conventional conversion mechanisms of the captured CO_2 (in the form of carbonate ions (CO_3^{2-})) in molten electrolytes can be described as follows (Deng et al., 2019; Yin et al., 2013):

Cathodic reactions:

$$CO_3^{2-} + 4e^- = C + 3O^{2-} \quad \text{(Equation 1)}$$

$$CO_3^{2-} + 2e^- = CO + 2O^{2-} \quad \text{(Equation 2)}$$

Anodic reaction on an inert anode:

$$2O^{2-} - 4e^- = O_2 \quad \text{(Equation 3)}$$

Supply of carbonate ions by CO_2 absorption:

$$O^{2-} + CO_2 = CO_3^{2-} \quad \text{(Equation 4)}$$

Overall reaction for CO_2 reduction according to Equations 1, 2, 3, and 4:

$$CO_2 = C + O_2 \quad \text{(Equation 5)}$$

$$CO_2 = CO + 1/2O_2 \quad \text{(Equation 5a)}$$

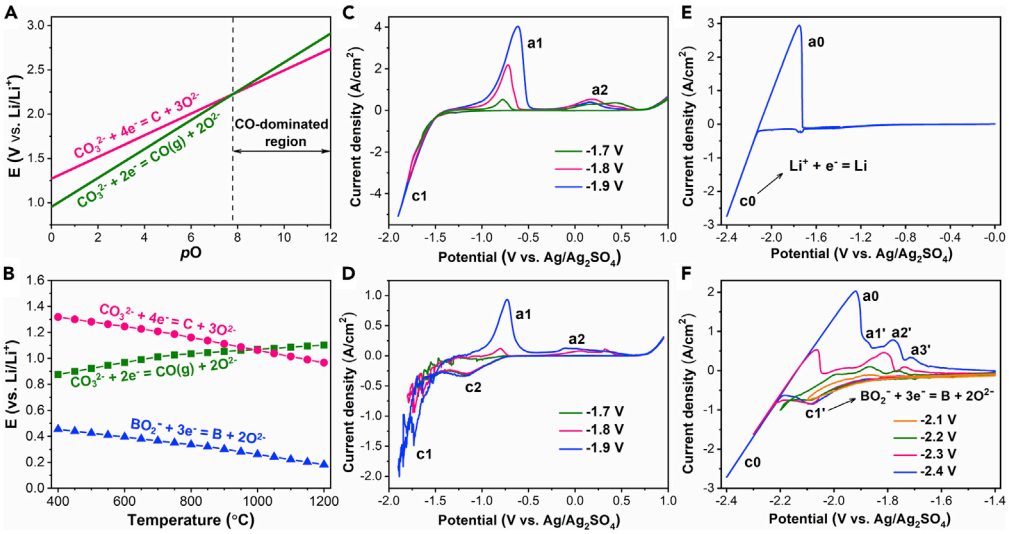

Figure 1. Thermodynamic Calculations and Electrochemical Measurements

(A) Correlation (E–*p*O) between reduction potential and oxygen anion concentration. $pO = -\log a_{O^{2-}}$.

(B) Thermodynamic calculations of possible cathodic reactions in molten LiCl–Li_2CO_3–$LiBO_2$.

(C and D) Cyclic voltammograms in molten LiCl–Li_2CO_3 (C) and molten LiCl–Li_2CO_3–$LiBO_2$ (D) with different scanning limits under Ar atmosphere at 550°C.

(E and F) Cyclic voltammograms in molten LiCl (E) and molten LiCl–1.25 mol% $LiBO_2$ (F) under Ar atmosphere at 650°C.

Considering the conventional cathodic process as presented in Equation 1, our hypothesis is that converting sequentially generated O^{2-} into other CO_2 absorbing species could theoretically decrease O^{2-} concentration (defined as alkalinity) in the electrolyte, which positively shifts reduction potential of absorbed CO_2 (i.e. CO_3^{2-}) according to the thermodynamic tendency based on Nernst equation, of which correlation between Nernstian potential (E) and alkalinity (aO^{2-}) is shown in Figure 1A. As can be clearly seen, the theoretical reduction potential of CO_3^{2-} producing carbon/CO can positively shift when the O^{2-} concentration is decreased. More interestingly, the selectivity toward CO_2RR product (such as carbon, CO) can also be regulated by controlling alkalinity of electrolyte during CO_2 electrolysis, because CO is preferentially generated due to more positive reduction potential toward CO than that toward carbon when O^{2-} concentration is greatly decreased (see CO-dominated region in Figure 1A).

From this perspective, we introduced BO_2^- (acting as O^{2-} acceptor) into the electrolyte to form BO_3^{3-} which showed excellent CO_2 absorption capacity to regenerate BO_2^- under CO_2 atmosphere (see Scheme 1) (Harada and Hatton, 2017), the mechanisms can be described as follows (Cherginets, 2005):

Conversion of electrochemically generated oxygen anions:

$$BO_2^- + O^{2-} \rightleftharpoons BO_3^{3-} \qquad \text{(Equation 6)}$$

Supply of carbonate ions and oxygen anion acceptors:

$$BO_3^{3-} + CO_2 \rightleftharpoons CO_3^{2-} + BO_2^- \qquad \text{(Equation 7)}$$

According to Lux–Flood acid–base theory (Flood and Förland, 1947; Lux, 1939), O^{2-} and BO_2^- (O^{2-} acceptor) can be regarded as base and acid, respectively, therefore BO_2^-/BO_3^{3-} is a conjugate acid–base pair as presented in Equation 6. Similar with buffer system theory in aqueous solution, the existence of BO_2^-/BO_3^{3-} in molten salt can buffer O^{2-} concentration, avoiding a sharp increase of alkalinity near cathode during CO_2 electrolysis. To be specific, the sequentially released O^{2-} during electroreduction of CO_3^{2-} can spontaneously combine with BO_2^- to form BO_3^{3-}, which can also act as CO_2 absorbent to produce CO_3^{2-} (electrochemical transformation precursor) and concurrently regenerate BO_2^- under CO_2 atmosphere, setting up a self-supply closed loop for sustainable buffering effect and durable CO_2RR.

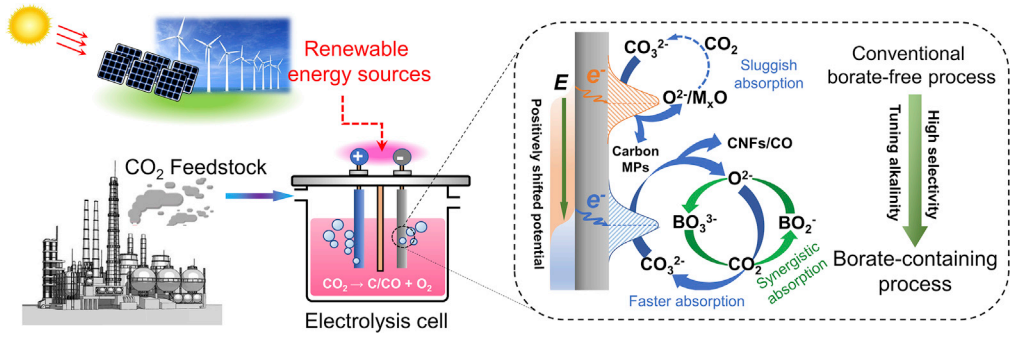

Scheme 1. Comparative Schematics of Borate-Enhanced Molten Salt Electrolysis Technology

To verify our hypothesis, molten LiCl–Li_2CO_3 (68.8:31.2 in molar ratio) was chosen as the electrolyte due to its simplex cation and relatively low melting point (517°C), $LiBO_2$ was accordingly chosen as O^{2-} acceptor to set up BO_2^-/BO_3^{3-} conjugate acid–base pair. The comparative analysis of cyclic voltammetry (CV), potentiostatic/galvanostatic electrolysis and long-term electrolysis were conducted in molten LiCl–Li_2CO_3–$LiBO_2$ compared to borate-free electrolyte using a homemade U-shape reactor equipped with an *in situ* gas analyzer (Figure S1).

As can be seen in Figure 1C, the cathodic peak c1 in borate-free electrolyte was attributed to the intrinsic reduction of CO_3^{2-} (Equation 1), which is consisent with previous observations (Yin et al., 2013; Ge et al., 2016a). Remarkably, the CV in borate-containing electrolyte showed an extra broad reduction peak c2 (see Figure 1D), of which potential was more positive than intrinsic reduction of CO_3^{2-} (peack c1). In accordance with our hypothesis, the appearance of peak c2 should be exclusively related to the positively shifted reduction of CO_3^{2-}, which was attributed to the BO_2^- buffering effect toward as-formed O^{2-} via Equations 8 and 9. Thermodynamic calculation (Figure 1B) as well as the CVs in LiCl (Figure 1E) and LiCl–$LiBO_2$ (Figure 1F) also confirm this observation because the reduction potential of borate was much more negative than that of CO_3^{2-}, indicating a promising electrochemial window of borate within the applied operating conditions.

Borate-assisted cathodic reactions:

$$CO_3^{2-} + 4e^- + 3BO_2^- = C + 3BO_3^{3-} \quad \text{(Equation 8)}$$

$$CO_3^{2-} + 2e^- + 2BO_2^- = CO + 2BO_3^{3-} \quad \text{(Equation 9)}$$

Oxidation of as-formed carbon during CV:

$$C + 2O^{2-} - 4e^- = CO_2 \quad \text{(Equation 10)}$$

As can be seen in Figures 1C and 1D, it should be noted that the oxidation peak a1 in LiCl–Li_2CO_3–$LiBO_2$, which was associated with sequentially released O^{2-} during CV scanning via Equation 10 (Ijije et al., 2014b), accounted for a much smaller charge quantity ratio between anodic peak and cathodic peak compared to that in LiCl–Li_2CO_3 (see Table 1) within identical scanning limit, suggesting a greatly decreased O^{2-} concentration due to the excellent buffering effect of BO_2^-/BO_3^{3-} toward O^{2-} via Equation 6. Similar observations were also found on different working electrodes, such as Mo, Ti, Cu, and graphite (Figure S2), showing an electrode-independent buffering effect related to BO_2^-/BO_3^{3-}, which is consistent with our hypothesis according to Nernst equation as presented in Figure 1A.

Effects of Borate on Cathodic Polarization and Product Distribution

To elucidate the reactions occurring at different potentials and to reveal the critical role of $LiBO_2$ toward product selectivity, the potentiostatic electrolysis was conducted on a plain Ni working electrode under Ar atmosphere. As can be seen in Figure 2A, neither obvious reduction current nor cathodic product (Figure 2C) was found in borate-free electrolyte below −1.0 V (vs. Ag/Ag_2SO_4). In the contrast, black deposits

Cathodic Limits	$LiCl–Li_2CO_3$			$LiCl–Li_2CO_3–LiBO_2$		
	Q_{c1} (C)	Q_{a1} (C)	Q_{a1}/Q_{c1}	Q_{c1+c2} (C)	Q_{a1} (C)	Q_{a1}/Q_{c1+c2}
−1.7 V	0.664	0.134	0.202	0.485	0	0
−1.8 V	1.467	0.623	0.425	0.656	0.019	0.029
−1.9 V	2.722	1.553	0.571	1.270	0.301	0.237

Table 1. The Charge Quantity Ratios between Anodic Peak (Q_a) and Cathodic Peak (Q_c) in Different Molten Electrolytes within Identical CV Scanning Potential Range

(i.e. carbon products, see Figure 2C) and noticeable reduction current (see Figure 2B) can be observed when applied potential was merely −0.8 V (vs. Ag/Ag_2SO_4) in borate-containing electrolyte. Specifically, the cathodic current density was over two times higher than that in $LiCl–Li_2CO_3$ at the same applied potential of −1.4 V (vs. Ag/Ag_2SO_4). Furthermore, the reduction potential was positively shifted by 400 mV to reach similar cathodic current density in borate-containing electrolyte compared to that in $LiCl–Li_2CO_3$ at −1.4 V (vs. Ag/Ag_2SO_4). Remarkably, the *in-situ* gas analyzer displayed that newly generated gaseous product species (i.e. CO, see Figure 2D) was commonly observed in borate-containing electrolyte during electrolysis, together with solid carbon products (see Figure 2C), which is clearly in accordance with our hypothesis and thermodynamic analysis. Whereas no CO but only solid carbon products were generated during the electrolysis within the investigated cathodic potential range (−1.0 to −1.4 V vs. Ag/Ag_2SO_4) in borate-free electrolyte, which is in good agreement with previous report (Ge et al., 2016a). Apparently, the distribution of CO_2RR products in molten $LiCl–Li_2CO_3–LiBO_2$ was also dependent on operating temperature and applied electrode potential (see Figure 2E), suggesting a highly tunable product selectivity toward CO_2RR. It is worth-mentioning that our finding further revealed that the CO content was significantly increased (see Figure 2D) and the yield can reach as high as ∼90% at a high current density (e.g. 100 mA/cm^2) by simply elevating electrolysis temperature (e.g. 650°C), where the current density for producing CO was at least 5 times higher than that in aqueous solution using noble metal catalysts (e.g. Au, Pd, <20 mA/cm^2) (Gao et al., 2015; Hall et al., 2015; Zhu et al., 2019). Furthermore, the electrode-independent high-yield CO production presented in this work was achieved at a relatively low temperature (650°C), exhibiting more advantages than previously reported molten salt electrolysis technology, in which the electrolysis temperature was as high as 900°C and a Ti cathode was exclusively used (Kaplan et al., 2010).

Considering that solid carbon is more preferentially obtained at 550°C (selectivity>90%), it is very interesting to find that nanostructures of carbon products can also be tailored in borate-containing electrolyte. To be specific, the SEM images of carbon products obtained in $LiCl–Li_2CO_3–LiBO_2$ illustrate that CNFs were commonly observed within −0.8 ∼ −1.4 V at 550°C (see Figures 3A–3D), accounting for at least 30% under respective electrolysis condition, whereas carbon products obtained in borate-free electrolyte were completely micron-scale quasi-spherical particles (Figure 3E), suggesting that borate can help regulate one-dimensional-oriented growth for carbon nucleis. Specifically, Figure 3B shows that the high-content (>80%) CNFs with diameter of ∼80 nm were observed. Considering that oxygen atoms play significant roles on carbon nanostructures, the growth of CNFs might be attributed to the *in situ* deoxidation via a buffering effect (Equation 6) during carbon nucleation, triggering the reforming of as-formed carbon atoms because lower oxygen content (see Table 2) and higher graphitic crystallinity (see higher G band in Figure 3B) were observed for CNFs compared to those for quasi-spherical particles. The critical role of oxygen removal on CNFs growth has also been reported by other work (Moyer et al., 2020), in which fast O_2 evolution originating from anodic process of O^{2-} at anode (Equation 3) is conducive to the growth of CNFs/CNTs. The findings in this work suggest the similar effort of O^{2-} removal; however, by a homogeneous process, where the borate in the electrolyte can help remove O^{2-} generated near cathode via Equation 6. In addition, it should be pointed out that no boron (B) was found in the obtained carbon products according to the X-ray photoelectron spectrometry (XPS) result (Table 2), suggesting the excellent thermodynamic stability of borates in the applied potential range, which was consistent with the observation in the CVs (Figure 1F).

The optimum conditions for producing high-yield either CO or CNFs were in good agreement with thermodynamic analysis (see Figures 1A and 1B), where elevating temperature and decreasing alkalinity of electrolyte can both give rise to a considerably high content of CO. Apparently, the performance that

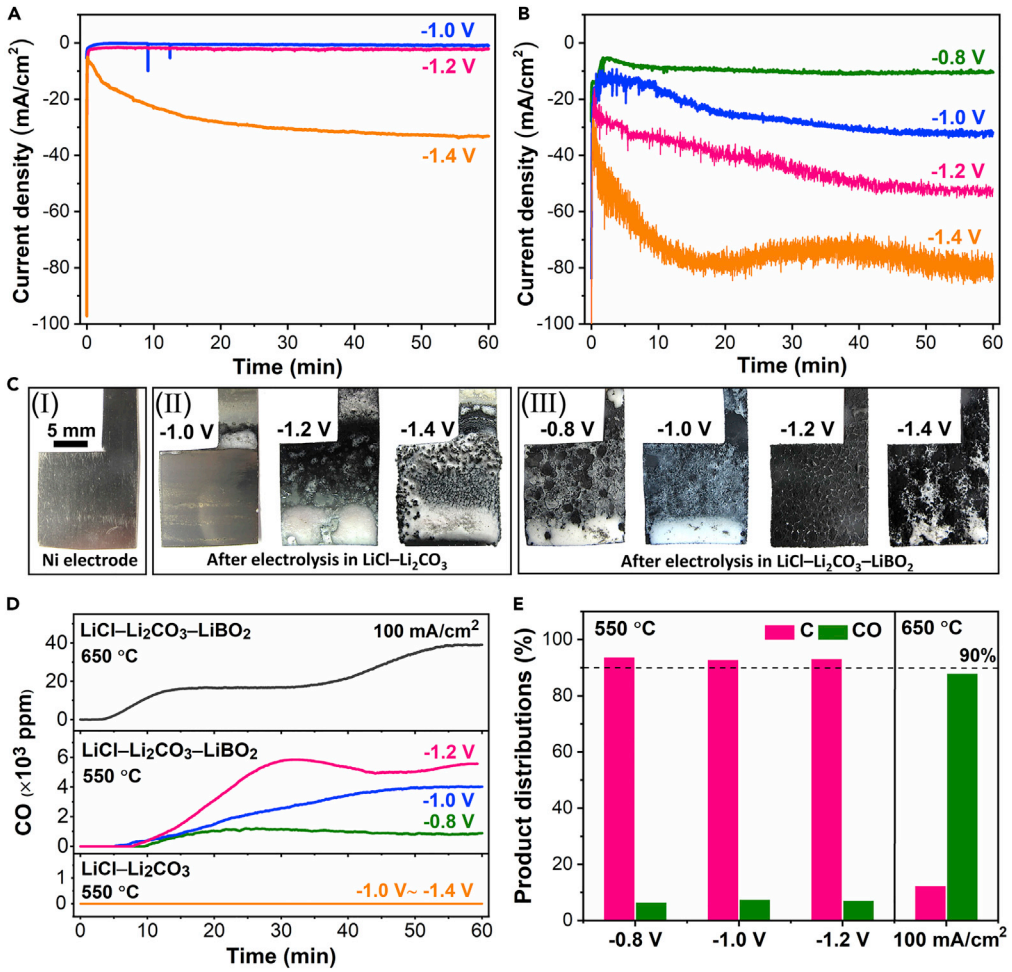

Figure 2. Potentiostatic Electrolysis and Product Distributions

(A and B) Current-time plots of potentiostatic electrolysis in (A) molten LiCl–Li_2CO_3 and (B) molten LiCl–Li_2CO_3–$LiBO_2$ under Ar atmosphere at 550°C.

(C) Corresponding optical images of Ni electrode before and after potentiostatic electrolysis.

(D) Detected CO content during potentiostatic and galvanostatic electrolysis.

(E) Product distributions in molten LiCl–Li_2CO_3–$LiBO_2$ under various conditions.

manipulating selectivity by tuning electrolyte alkalinity is also associated with borate concentration, which needs further investigation in the future.

Effects of Borate on Cathodic Passivation and CO_2 Conversion Efficiency

Cathodic passivation effect:

$$2Li^+ + O^{2-} \rightleftharpoons Li_2O\ (s) \qquad \text{(Equation 11)}$$

Poor CO_2 capture by solid Li_2O:

$$Li_2O\ (s) + CO_2\ (g) = Li_2CO_3\ (s) \qquad \text{(Equation 12)}$$

As shown in Equation 11, cathodic passivation effect usually results from accumulation of solid oxides (e.g. Li_2O) on cathode, of which solubility in molten electrolytes is limited (Gao et al., 2018), leading to an increasing cathodic polarization because of the undesirable electric resistance of covered oxides (Gao et al., 2018; Deng et al., 2019), which also retard both CO_2 capture (Equation 12) and sequential

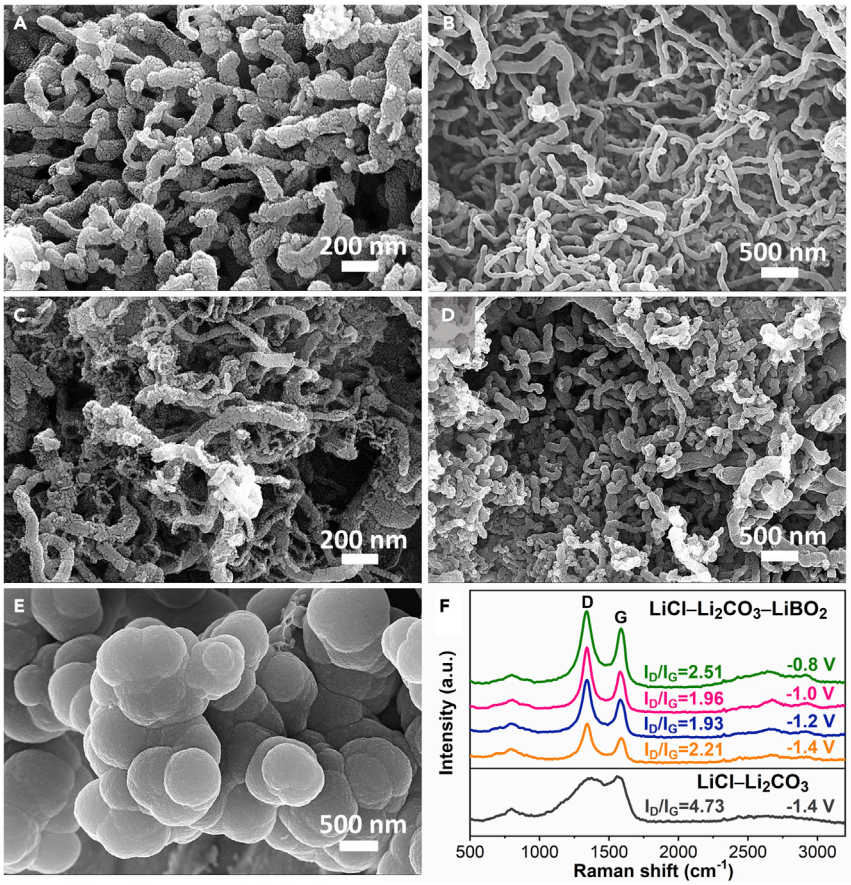

Figure 3. SEM and Raman Characterization of Carbon Products

(A–D) SEM image of carbon products obtained under potentiostatic electrolysis at (A) −0.8 V, (B) −1.0 V, (C) −1.2 V and (D) −1.4 V in molten LiCl–Li_2CO_3–$LiBO_2$.

(E) SEM images of carbon product obtained under potentiostatic electrolysis at −1.4 V in molten LiCl–Li_2CO_3.

(F) Raman spectrums of carbon products obtained in different molten electrolytes.

electrotransformation. To further verify the positive effort inhibiting cathodic passivation effect when borate is added into the electrolyte, the galvanostatic electrolysis at a high cathodic current density (e.g. 260 mA/cm^2) was carried out in molten LiCl–Li_2CO_3–$LiBO_2$ and molten LiCl–Li_2CO_3 with identical electrolysis duration, respectively. It has been previously reported that Li_2O content on raw cathode after electrolysis is an indicator to the degree of passivation effect, where higher current density can preferentially lead to more severe cathodic passivation effect while higher Li_2O content on raw cathode can be observed (Gao et al., 2018). Therefore, after the electrolysis, the raw cathodic products were analyzed by X–ray diffraction spectroscopy (XRD) without any post-treatment. As shown in Figure 4A, the XRD patterns clearly show that cathodic passivation effect was greatly inhibited in borate-containing electrolyte, because a much lower relative intensity (I_{Li2O}:I_{melt}) of Li_2O was observed, which is consistent with our hypothesis that borate can remove O^{2-} in the electrolyte via Equation 6.

From the perspective of practical application, a mixed gas containing 14 vol% CO_2 (the same CO_2 content as flue gas) and Ar was bubbled into the melt. To gain a further insight into the efforts of borate buffer system on overall energy consumption, long-term working stability and CO_2 conversion efficiency, the variations of cell voltage and outlet CO_2 concentration during galvanostatic electrolysis were real-time monitored for 18 h. As can be seen in Figure 4B, the applied cell voltage for CO_2RR in molten LiCl–Li_2CO_3–$LiBO_2$ was 600 mV lower than that in molten LiCl–Li_2CO_3 under the same cathodic current density (e.g. 23 mA/cm^2), merely accounting for approximately 60% of electrolysis energy consumption in molten borate-free electrolyte. Considering that small motive Li^+ cations dominate electrical conductivity in Li-rich

Element (Atom%)	$LiCl–Li_2CO_3–LiBO_2$				$LiCl–Li_2CO_3$
	−0.8 V	−1.0 V	−1.2 V	−1.4 V	−1.4 V
C	94.06	96.03	95.68	95.51	83.25
O	5.52	3.97	4.10	4.25	14.34
B	0	0	0	0	0
Ti	0	0	0	0	0
Ni	0.42	0	0.22	0.24	2.41

Table 2. The XPS Analysis of Carbon Products Obtained under Potentiostatic Electrolysis in Different Molten Electrolytes

molten species (Katsumata et al., 1999a, 1999b), therefore, the influence of electrical conductivity in molten salt with and without $LiBO_2$ might be marginal in this work because Li^+ is the only cation in the selected molten electrolyte. Given the consideration above, the positively shifted cathodic potential and the inhibited cathodic passivation effect in borate-containing electrolyte should be responsible for the much lower applied cell voltage.

As shown in Figure 4B, the slightly fluctuated variation of cell voltage demonstrated a long-lasting operating stability for borate-assisted CO_2RR. More importantly, according to the contrast of CO_2 outlet concentration (Figure 4B), it is interesting to find that the CO_2 conversion efficiency in molten $LiCl–Li_2CO_3–LiBO_2$ was over three times higher than that in $LiCl–Li_2CO_3$. The increasing amount of CO_2 absorbing species and inhibited cathodic passivation effect in borate-containing molten electrolyte should both be responsible for the lower CO_2 outlet concentration. Specifically, for borate-free electrolyte, O^{2-} acting as CO_2 absorbent was sequentially generated during CO_2RR via Equation 1, whereas cathodic passivation effect easily occurred when O^{2-} was oversaturated (Equation 11), leading to precipitation of solid Li_2O on cathodes together with poor CO_2 absorption performance (Equation 12). By contrast, for borate-containing electrolyte, owing to the buffering effect of borates toward O^{2-}, the cathodic passivation effect can be effectively inhibited due to the O^{2-} removal by Equation 6, instead, a more soluble high-performance CO_2 absorbing species (i.e. BO_3^{3-}) was generated, which can regenerate BO_2^- and concurrently produce CO_3^{2-} under CO_2 atmosphere (Equation 7). Therefore, the CO_2 absorption performance of overall CO_2 absorbing species (BO_3^{3-} and O^{2-}) in borate-containing electrolyte was better than those (mainly O^{2-}, solid Li_2O) in borate-free electrolyte. In other words, the synergistic CO_2 absorption in borate-containing electrolyte showed superior advantage regarding CO_2 capture and conversion efficiency, achieving a three-time higher CO_2 conversion efficiency under identical current density in comparison with borate-free electrolyte. The gradually decreased but eventually stable CO_2 outlet concentration for borate-containing electrolyte (see Figure 4B) indicates that the acid–base equilibrium involving Equations 6, 7, 8, and 9 was proceeding during the electrolysis.

To gain more insights into the advantages of this work, a comparative analysis based on the benchmarking of molten salt CO_2RR regarding cathodic potential, energy consumption and reaction conditions in different electrolytes is listed in Table S1. Remarkably, it should be pointed out that the presented borate-containing electrolyte in this work exhibited more positive onset potential related to CO_2RR, suggesting a more favorable energy demand. More interestingly, the cathodic potential in borate-containing electrolyte was much more positive than other reported electrolysis systems, which can be clearly observed under identical operating condition (i.e. 35 mA/cm^2, 550°C) using the same electrodes, indicating a higher energy efficiency. Accordingly, the both much lower cell voltage and energy consumption for producing solid carbon product by reducing 1 kg of CO_2 further confirmed the benefits of CO_2RR in borate-containing electrolyte. More importantly, with the assistance of borate, the extended gaseous product (i.e. CO) with a high faradaic efficiency of ~90% was achieved, whilst the operating temperature and the applied cell voltage both were much lower than previously reported work under optimum conditions. Regarding positively shifted reduction potential, lower energy consumption and tunable product selectivity, achieving CO_2RR in borate-containing electrolyte under mild operating conditions exhibits superior advantages than conventional borate-free processes.

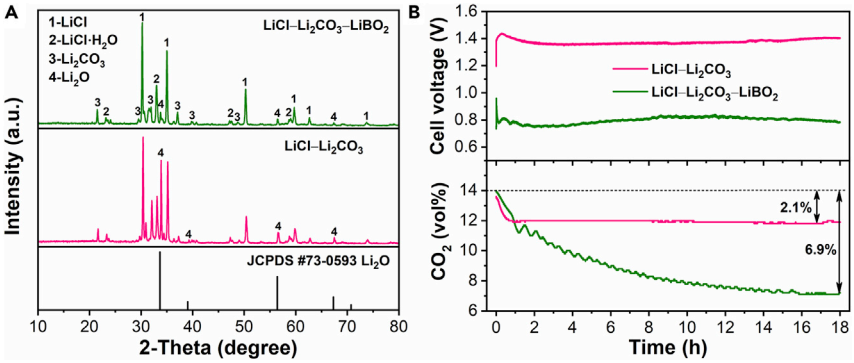

Figure 4. Effects of Borate on Cathodic Passivation and CO_2 Conversion Efficiency

(A) XRD patterns of raw cathodic products after galvanostatic electrolysis at 260 mA/cm^2 in different molten electrolytes under 550°C.

(B) Variations of cell voltage and outlet CO_2 concentration during galvanostatic electrolysis at 23 mA/cm^2 in different molten electrolytes under 550°C.

The long-term stability of borate buffering system during CO_2RR is the prerequisite in the viewpoint of practical application. Similar with classical acid–base buffering systems in aqueous solution, the buffering capacity of BO_2^-/BO_3^{3-} pairs is dependent on the concentration of borates. For a given borate buffer concentration (e.g. 5 mol% $LiBO_2$ in this work), the buffering effect toward base (O^{2-}) might not work well if the as-formed O^{2-} concentration was too high, which is related to the inharmonic electrolysis parameters (such as high current density or high cell voltage) because the amount of sequentially generated O^{2-} during electrolysis is beyond the buffering capacity of BO_2^-/BO_3^{3-} pairs. To ensure the stability of buffer system, it is also important to precisely control the applied cathodic polarization within the potential range of which borates may not be reduced. Considering that the sustainable supply of BO_2^- is available via CO_2 absorption (Equation 7), therefore, the CO_2 atmosphere and suitable operating temperature are other important factors contributing to sustaining BO_2^-/BO_3^{3-} pairs. Given the considerations above, the long-term stability of borate-assisted electrolysis presented in this work can be guaranteed under CO_2 atmosphere and at a moderate current density (e.g. 23 mA cm^{-2} in Figure 4B).

Conclusion

We demonstrate a facile strategy to manipulate CO_2RR selectivity at a positively shifted reduction potential by regulating electrolyte alkalinity, which is associated with the buffering effect of borate. Specifically, the as-formed borate conjugate acid–base pair can effectively buffer the concentration of electrochemically generated O^{2-} in the electrolyte, avoiding a sharp increase of alkalinity and concurrently inhibiting cathodic passivation effect during CO_2RR. Owing to the borate buffering effect toward electrolyte alkalinity, a newly extended product species (i.e. CO) was achieved, of which selectivity (either CO or CNFs) was highly tunable by simply regulating electrolysis conditions. In particular, ~90% CO can be obtained at a high current density (e.g. 100 mA/cm^2). It was further revealed that introducing borate into the electrolyte is conducive to transforming pristine CO_2-derived carbon quasi-spherical particles into CNFs. In comparison with CO_2RR in borate-free electrolyte, the overall energy consumption of borate-assisted process can be decreased by 40%, while the CO_2 conversion efficiency can be increased by 300%. The findings not only give clues to extending CO_2RR product species under mild operating condition but also provide a feasible pathway to achieve carbon-neutral cycle at a higher energy efficiency.

Limitations of the Study

This work provides a borate-assisted strategy to navigate CO_2RR pathway by controlling electrolyte alkalinity. Restrained by the cathodic limitation of borates, it is currently difficult to achieve CO_2RR at a considerably higher current density within limited electrochemical window. Hence, a more electrochemically stable buffer system should be developed in the future.

Resource Availability

Lead Contact

Further information and requests for resources and reagents should be directed to and will be fulfilled by the Lead Contact, Dihua Wang (wangdh@whu.edu.cn).

Materials Availability

This study did not generate new unique reagents.

Data and Code Availability

The data that support the findings of this study are available from corresponding author upon reasonable request.

METHODS

All methods can be found in the accompanying Transparent Methods supplemental file.

SUPPLEMENTAL INFORMATION

Supplemental Information can be found online at https://doi.org/10.1016/j.isci.2020.101607.

ACKNOWLEDGMENTS

This work was funded by National Natural Science Foundation of China (No. 21673162), China Postdoctoral Science Foundation (No. 2019M652708).

AUTHOR CONTRIBUTIONS

L.H. and B.D. contributed equally. Conceptualization and Writing – Original Draft, L.H., B.D.; Formal Analysis, B.D., D.W., K.D.; Visualization, R.J., Y.D.; Methodology, L.H., B.D., D.W.; Funding Acquisition, D.W., B.D.

DECLARATION OF INTERESTS

The authors declare no competing interests.

Received: June 11, 2020
Revised: August 26, 2020
Accepted: September 21, 2020
Published: October 23, 2020

REFERENCES

Chen, K.-J., Yang, Q.-Y., Sen, S., Madden, D.G., Kumar, A., Pham, T., Forrest, K.A., Hosono, N., Space, B., Kitagawa, S., and Zaworotko, M.J. (2018). Efficient CO_2 removal for ultra-pure CO production by two hybrid ultramicroporous materials. Angew. Chem. Int. Ed. *57*, 3332–3336.

Chen, Y., and Mu, T. (2019). Conversion of CO_2 to value-added products mediated by ionic liquids. Green. Chem. *21*, 2544–2574.

Cherginets, V.L. (2005). Oxoacidity: reactions of oxo-compounds in ionic solvents (Elsevier).

Chery, D., Albin, V., Lair, V., and Cassir, M. (2014). Thermodynamic and experimental approach of electrochemical reduction of CO_2 in molten carbonates. Int. J. Hydrogen Energy *39*, 12330–12339.

Deng, B., Gao, M., Yu, R., Mao, X., Jiang, R., and Wang, D. (2019). Critical operating conditions for enhanced energy-efficient molten salt CO_2 capture and electrolytic utilization as durable looping applications. Appl. Energy *255*, 113862.

Deng, B., Mao, X., Xiao, W., and Wang, D. (2017). Microbubble effect-assisted electrolytic synthesis of hollow carbon spheres from CO_2. J. Mater. Chem. A *5*, 12822–12827.

Deng, B., Tang, J., Gao, M., Mao, X., Zhu, H., Xiao, W., and Wang, D. (2018). Electrolytic synthesis of carbon from the captured CO_2 in molten LiCl–KCl–$CaCO_3$: critical roles of electrode potential and temperature for hollow structure and lithium storage performance. Electrochim. Acta *259*, 975–985.

Douglas, A., Carter, R., Muralidharan, N., Oakes, L., and Pint, C.L. (2017). Iron catalyzed growth of crystalline multi-walled carbon nanotubes from ambient carbon dioxide mediated by molten carbonates. Carbon *116*, 572–578.

Flood, H., and Förland, T. (1947). The acidic and basic properties of oxides. Acta Chem. Scand. *1*, 592–604.

Gao, D., Zhou, H., Wang, J., Miao, S., Yang, F., Wang, G., Wang, J., and Bao, X. (2015). Size-dependent electrocatalytic reduction of CO_2 over pd nanoparticles. J. Am. Chem. Soc. *137*, 4288–4291.

Gao, M., Deng, B., Chen, Z., Tao, M., and Wang, D. (2018). Cathodic reaction kinetics for CO_2 capture and utilization in molten carbonates at mild temperatures. Electrochem. Commun. *88*, 79–82.

Ge, J., Hu, L., Song, Y., and Jiao, S. (2016a). An investigation into the carbon nucleation and growth on a nickel substrate in LiCl-Li_2CO_3 melts. Faraday Discuss. *190*, 259–268.

Ge, J., Wang, S., Hu, L., Zhu, J., and Jiao, S. (2016b). Electrochemical deposition of carbon in LiCl–NaCl–Na_2CO_3 melts. Carbon *98*, 649–657.

Hall, A.S., Yoon, Y., Wuttig, A., and Surendranath, Y. (2015). Mesostructure-induced selectivity in CO_2 reduction catalysis. J. Am. Chem. Soc. *137*, 14834–14837.

Harada, T., and Hatton, T.A. (2017). Tri-lithium borate (Li_3BO_3); a new highly regenerable high capacity CO_2 adsorbent at intermediate temperature. J. Mater. Chem. A. *5*, 22224–22233.

He, M., Sun, Y., and Han, B. (2013). Green carbon science: scientific basis for integrating carbon resource processing, utilization, and recycling. Angew. Chem. Int. Ed. *52*, 9620–9633.

Hu, L., Song, Y., Ge, J., Zhu, J., and Jiao, S. (2015). Capture and electrochemical conversion of CO_2 to ultrathin graphite sheets in $CaCl_2$-based melts. J. Mater. Chem. A *3*, 21211–21218.

Ijije, H.V., Lawrence, R.C., Siambun, N.J., Jeong, S.M., Jewell, D.A., Hu, D., and Chen, G.Z. (2014a). Electro-deposition and re-oxidation of carbon in carbonate-containing molten salts. Faraday Discuss. *172*, 105–116.

Ijije, H.V., Sun, C., and Chen, G.Z. (2014b). Indirect electrochemical reduction of carbon dioxide to carbon nanopowders in molten alkali carbonates: process variables and product properties. Carbon *73*, 163–174.

Jiang, R., Gao, M., Mao, X., and Wang, D. (2019). Advancements and potentials of molten salt CO_2 capture and electrochemical transformation (MSCC-ET) process. Curr. Opin. Electrochem. *17*, 38–46.

Kaplan, V., Wachtel, E., Gartsman, K., Feldman, Y., and Lubomirsky, I. (2010). Conversion of CO_2 to CO by electrolysis of molten lithium carbonate. J. Electrochem. Soc. *157*, B552–B556.

Katsumata, T., Suzuki, N., Shibasaki, M., and Matsuo, T. (1999a). Electrical conductivity and nuclear magnetic resonance of molten lithium borates. ECS Proc. *1999–41*, 383–391.

Katsumata, T., Suzuki, N., Shibasaki, M., and Matsuo, T. (1999b). Electric field application to molten lithium borates. In Materials Research in Low Gravity II, N. Ramachandran, ed., pp. 242–249.

König, M., Vaes, J., Klemm, E., and Pant, D. (2019). Solvents and supporting electrolytes in the electrocatalytic reduction of CO_2. iScience *19*, 135–160.

Licht, S., Douglas, A., Ren, J., Carter, R., Lefler, M., and Pint, C.L. (2016). Carbon nanotubes produced from ambient carbon dioxide for environmentally sustainable lithium-ion and sodium-ion battery anodes. ACS Cent. Sci. *2*, 162–168.

Liu, S., Lu, X.F., Xiao, J., Wang, X., and Lou, X.W.D. (2019). Bi_2O_3 nanosheets grown on multi-channel carbon matrix to catalyze efficient CO_2 electroreduction to HCOOH. Angew. Chem. Int. Ed. *58*, 13828–13833.

Lux, H. (1939). "Säuren" und "Basen" im Schmelzfluss: die Bestimmung der Sauerstoffionen-Konzentration. Z. für Elektrochemie Angew. Phys. Chem. *45*, 303–309.

MacDowell, N., Florin, N., Buchard, A., Hallett, J., Galindo, A., Jackson, G., Adjiman, C.S., Williams, C.K., Shah, N., and Fennell, P. (2010). An overview of CO_2 capture technologies. Energy Environ. Sci. *3*, 1645–1669.

Moyer, K., Zohair, M., Eaves-Rathert, J., Douglas, A., and Pint, C.L. (2020). Oxygen evolution activity limits the nucleation and catalytic growth of carbon nanotubes from carbon dioxide electrolysis via molten carbonates. Carbon *165*, 90–99.

Ren, J., Li, F.-F., Lau, J., González-Urbina, L., and Licht, S. (2015). One-pot synthesis of carbon nanofibers from CO_2. Nano Lett. *15*, 6142–6148.

Rosen, B.A., Salehi-Khojin, A., Thorson, M.R., Zhu, W., Whipple, D.T., Kenis, P.J.A., and Masel, R.I. (2011). Ionic liquid-mediated selective conversion of CO_2 to CO at low overpotentials. Science *334*, 643–644.

Song, Y., Zhang, X., Xie, K., Wang, G., and Bao, X. (2019). High-temperature CO_2 electrolysis in solid oxide electrolysis cells: developments, challenges, and prospects. Adv. Mater. *31*, 1902033.

Sun, Z., Liu, C., Lu, G., Song, X., Sun, S., Sun, Y., and Yu, J. (2011). Coupled thermoelectric model and effects of current fluctuation on thermal balance in magnesium electrolysis cell. Energy Fuels *25*, 2655–2663.

Sysoev, I.A., Ershov, V.A., and Kondrat'ev, V.V. (2015). Method of controlling the energy balance of electrolytic cells for aluminum production. Metallurgist *59*, 518–525.

Wu, H., Ji, D., Li, L., Yuan, D., Zhu, Y., Wang, B., Zhang, Z., and Licht, S. (2016). A New technology for efficient, high yield carbon dioxide and water transformation to methane by electrolysis in molten salts. Adv. Mater. Technol. *1*, 1600092.

Wu, W., Ding, H., Zhang, Y., Ding, Y., Katiyar, P., Majumdar, P.K., He, T., and Ding, D. (2018). 3D self-architectured steam electrode enabled efficient and durable hydrogen production in a proton-conducting solid oxide electrolysis cell at temperatures lower than 600 °C. Adv. Sci. *5*, 1800360.

Yin, H., Mao, X., Tang, D., Xiao, W., Xing, L., Zhu, H., Wang, D., and Sadoway, D.R. (2013). Capture and electrochemical conversion of CO_2 to value-added carbon and oxygen by molten salt electrolysis. Energy Environ. Sci. *6*, 1538–1545.

Zhu, D.D., Liu, J.L., and Qiao, S.Z. (2016). Recent advances in inorganic heterogeneous electrocatalysts for reduction of carbon dioxide. Adv. Mater. *28*, 3423–3452.

Zhu, S., Qin, X., Wang, Q., Li, T., Tao, R., Gu, M., and Shao, M. (2019). Composition-dependent CO_2 electrochemical reduction activity and selectivity on Au-Pd core-shell nanoparticles. J. Mater. Chem. A *7*, 16954–16961.

iScience, Volume *23*

Supplemental Information

Tunable Selectivity and High Efficiency of CO_2 Electroreduction via Borate-Enhanced Molten Salt Electrolysis

Liangyou Hu, Bowen Deng, Kaifa Du, Rui Jiang, Yanpeng Dou, and Dihua Wang

Supplemental Figures and Tables

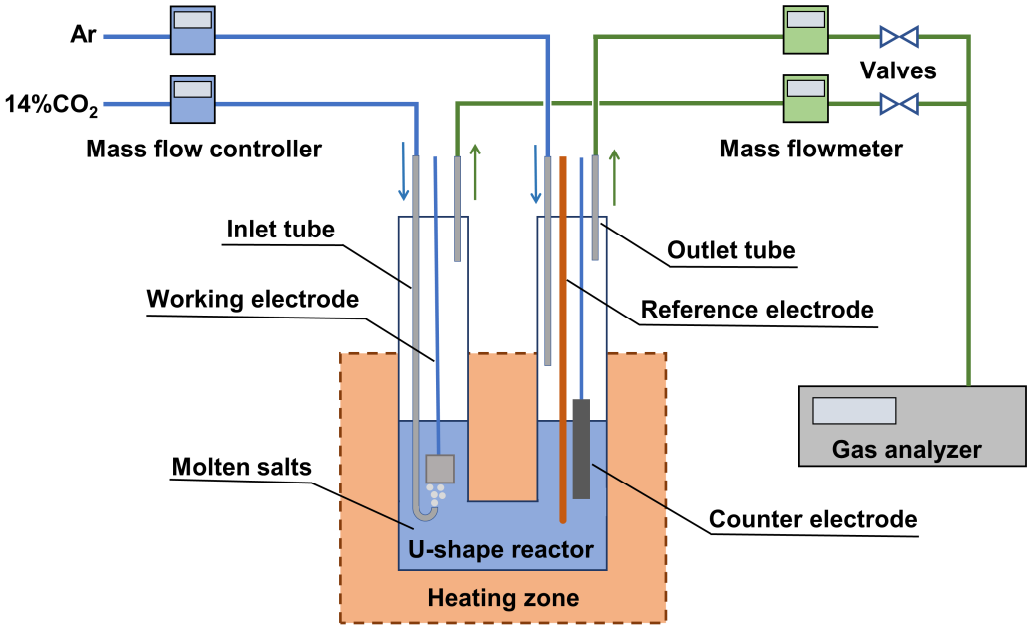

Figure S1. The schematic of home-made U-shape reactor equipped with *in-situ* gas analyzer. Related to Figure 1.

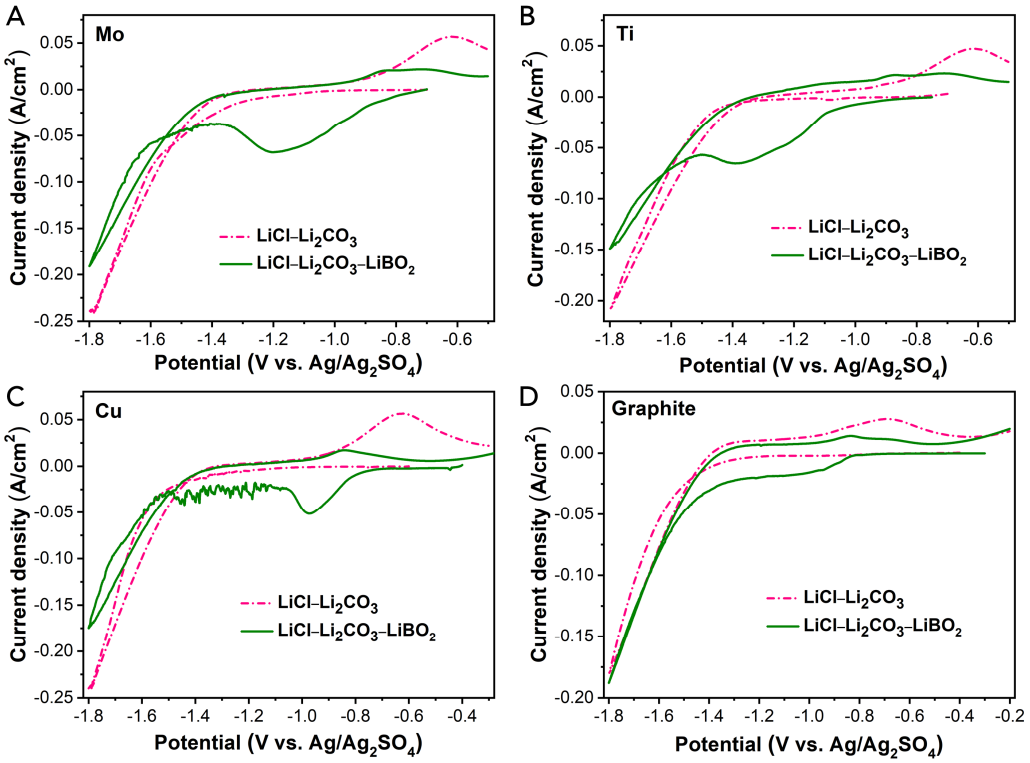

Figure S2. Cyclic voltammograms on different working electrodes in molten LiCl–Li_2CO_3–$LiBO_2$ and molten LiCl–Li_2CO_3. Related to Figure 1.

Table S1. The comparative analysis based on benchmarking of reported molten salt CO_2 electrolysis processes. Related to Figure 1.

Electrolyte	T (°C)	Onset potential (V vs. Li/Li^+)	Cathode	Anode	Current density (mA/cm^2)	Corresponding cathodic potential (V vs. Li/Li^+)	Cell voltage (V)	Faradaic efficiency	Energy consumption (kWh/kg_{CO_2})	Dominated products	Reference
$LiCl-Li_2CO_3-LiBO_2$	550	1.40	Ni	Graphite	35	1.15	0.90	93.8%	2.34	CNFs	This work
$LiCl-Li_2CO_3$	550	0.90	Ni	Graphite	35	0.75	1.53	~80%	~4.66	Carbon particles	This work
$LiCl-KCl-CaCO_3$	550	1.10	Ni	Graphite	35	0.50	2.80	81.6%	~7.63	Hollow Carbon spheres	Deng et al., 2017; Deng et al., 2018
$Li_2CO_3–Na_2CO_3–K_2CO_3$	500	0.40	Ni	SnO_2	40	–	3.00	74%	10.35	Carbon particles	Yin et al., 2013
$LiCl-KCl-Li_2CO_3$	450	1.10	Ni	Graphite	100	–	3.85	76%	–	Carbon sheets	Deng et al., 2016
$CaO-CaCl_2$	900	–	Graphite	Graphite	100		3.10	–	–	Carbon particles	Kikuchi et al., 2015
$LiCl-Li_2CO_3-LiBO_2$	650	–	Ni	Graphite	100	–	0.42	~90%	0.61	CO	This work
Li_2CO_3	900	–	Ti	Graphite	100	–	1.00	97.2%	1.34	CO	Kaplan et al., 2010; Küngas, 2020
$CaO-CaCl_2$	900	–	Stainless steel	ZrO_2	50	–	3.10	~85%	–	CO	Matsuura et al., 2015

Transparent Methods

Materials and electrochemical measurements

Anhydrous LiCl (≥99.0%), Li_2CO_3 (≥99.0%), $LiBO_2$ (≥99.99%) were purchased from Aladdin Biochemical Technology Co., Ltd, China. 1800 g of LiCl–Li_2CO_3 (68.8:31.2 mol%) with and without 5 mol% $LiBO_2$ were placed into a home-made U-shape reactor equipped with *in-situ* gas analyzer, of which schematic diagram is presented in Fig. S1. The salt mixtures were dried at 200 °C under Ar for 24 h to remove the adhered moisture before heating up to the target temperature. The cyclic voltammetry in LiCl–Li_2CO_3 and LiCl–Li_2CO_3–$LiBO_2$ were conducted on an electrochemical workstation (CHI1140A, CH Instrument, Inc., USA) under Ar atmosphere at 550 °C, the scan rate was 50 mV/s. To elucidate the electrochemical process occurring on the different electrodes, a Pt wire (contact area of 0.071 cm^2), a graphite plate (contact area of 4.5 cm^2) as well as plain transition-metal sheets (contact area of 4.5 cm^2) such as Mo, Ti and Cu were used as working electrodes, and a graphite rod (contact area of 22 cm^2) served as a counter electrode. The reference electrode was a silver wire (1mm in diameter) placed in a sealed alumina tube, which was filled with 0.1 mol/kg Ag_2SO_4-containing Li–Na–K carbonates (43.5:31.5:25 mol%). For comparison, the cyclic voltammetry was also tested in molten LiCl with and without 1.25 mol% $LiBO_2$ under Ar atmosphere on a Pt wire working electrode (contact area of 0.32 cm^2), which was conducted at 650 °C due to the limited melting point (605 °C) of LiCl. The scan rate was 100 mV/s.

Potentiostatic and galvanostatic electrolysis

The potentiostatic and galvanostatic electrolysis were also conducted on an electrochemical workstation (CHI1140A, CH Instrument, Inc., USA) in above-mentioned U-shape reactor containing LiCl–Li_2CO_3 (68.8:31.2 mol%) with and without 5 mol% $LiBO_2$. The inlet gas flows

of the working electrode (cathode) chamber and counter electrode (anode) chamber were controlled by mass flow controller (FMA5400A series, OMEGA Engineering, Inc., USA), the corresponding outlet gas flows were measured by mass flow meter (FMA1700A series, OMEGA Engineering, Inc., USA). Pure CO_2 (500 mL/min) was bubbled into the melts for 6 h before electrolysis to keep the same initial equilibrium state of the melts.

A Ni sheet (1.5 cm×1.5 cm) and a graphite rod (20 mm in diameter, contact area of 22 cm^2) served as the working electrode and the counter electrode, respectively. For potentiostatic electrolysis, a flow (50 mL/min) of Ar was purged into the chambers to keep inert atmosphere. For galvanostatic electrolysis, a flow (50 mL/min) of 14%CO_2-Ar mixed gas was bubbled into the melts below the working electrode by a Ti inlet-tube (6 mm in diameter), and the applied cell voltage was real-time monitored on a Neware DC power system (CT-3008-10V10A, Shenzhen Neware Electronic Co., Ltd., China). During the potentiostatic and galvanostatic electrolysis, all of the outlet gases from the working electrode (cathode) chamber were real-time detected by *in-situ* gas analyzer (AGA1000, Nanjing AE Technology Co., Ltd., China) with Non-Dispersive Infrared (NDIR) detector.

Characterizations of obtained carbon products

After the electrolysis, the cathodic products obtained in different molten electrolytes were rinsed with 1 M HCl and distilled water to remove the adhered frozen electrolyte, and were further dried in a vacuum oven at 80 °C for 12 h. Afterwards, the obtained carbon products were characterized by scanning electron microscopy (SEM, Zeiss SIGMA), X–ray diffraction spectroscopy (XRD, Shimadzu X–ray 6000 with Cu Kα radiation at 40 kV and 250 mA, λ=0.154 nm, Japan), Laser Confocal Raman Microspectroscopy (Renishaw RM1000, UK) at room temperature with an excitation wavelength at 532 nm from a diode pumped solid–state laser and

a Micromeritics ASAP 2020 automatic analyzer at liquid N_2 temperature, and elemental analysis was evaluated by X-ray photoelectron spectrometry (XPS, ESCALAB 250Xi).

Standard Nernstian potential

$$CO_3^{2-}+4e^-= C+3O^{2-} \quad (S1)$$

$$CO_3^{2-}+2e^-= CO+2O^{2-} \quad (S2)$$

$$BO_2^-+3e=B+2O^{2-} \quad (S3)$$

The standard reduction potential of different cathodic reactions (Eq. S1–S3) were calculated according to thermodynamic equation as presented following:

$$E_0 = \frac{\Delta G}{nF} \quad (S4)$$

where E_0 represents for standard potential, n and F denotes to electron transfer number and Faraday constant (96500 C/mol), respectively. ΔG stands for Gibbs free energy change for different reactions, gaining from HSC 6.0 software.

Correlation between Nernstian potential and alkalinity

The correlations between theoretical reduction potentials and oxygen anion concentrations for Eq. (S1) and Eq. (S2) were fitted by following Nernst Equations, respectively:

$$E = E_0 + \frac{2.303RT}{nF} \cdot log \frac{a_{CO_3^{2-}}}{(a_{O^{2-}})^3} = E_0 - \frac{3 \cdot 2.303RT}{nF} \log a_{O^{2-}} \quad (S5)$$

$$E = E_0 + \frac{2.303RT}{nF} \cdot log \frac{a_{CO_3^{2-}}}{\frac{P_{CO}}{P_{atm}}(a_{O^{2-}})^2} = E_0 - \frac{2 \cdot 2.303RT}{nF} \log a_{O^{2-}} \quad (S6)$$

where E represents for equilibrium potential, $a_{O^{2-}}$ and $a_{CO_3^{2-}}$ refer to oxygen anion concentration and carbonate ion concentration, respectively. P_{CO} and P_{atm} denote to CO partial pressure and standard atmosphere pressure (101.325 kPa), respectively. In order to simplify the

discussion and calculation of theoretical Nernstian potential based on the only variate ($a_{O^{2-}}$), therefore, $a_{CO_3^{2-}}$ and P_{CO} are assumed to be under standard state, which can show the intrinsic thermodynamic tendency related to $a_{O^{2-}}$. Although this assumption might be far away from what it really was, it would not change the consequence of thermodynamic tendency. Actually, the much lower actual partial pressure of generated CO (approaching to zero at the very beginning of reaction, far away from standard state of 1 atm) can lead to a much more positive shift of actual reduction potential than theoretical potential.

Product distributions

Attributed to that CO_2RR was the only electrochemical reaction taking place within all the investigated conditions, therefore, either gaseous CO or solid carbon was the cathodic products. Due to the observing fact that carbon deposits were easily peeled off from the cathodes and were immersed into the melt when CO was generated, it was difficult to completely collect all of the solid carbon products. Therefore, the distribution of carbon was evaluated by the distribution of CO which was precisely calculated according to the real-time recorded CO content. The equations are displayed as follows:

$$\delta_{CO} + \delta_{carbon} = 1 \tag{S7}$$

$$\delta_{CO} = \frac{Q_{CO}}{Q} \tag{S8}$$

$$Q_{CO} = \frac{n \cdot F \cdot \mu \cdot \int_0^t c dt}{1000V^*} \tag{S9}$$

where δ_{CO} and δ_{carbon} refer to distribution fraction of CO and solid carbon, respectively. Q_{CO} and Q denote to charge transfer quantities of obtained CO and overall electrolysis, respectively. F and n stand for Faraday constant (96500 C/mol) and electron transfer number, respectively. For

CO, n=2. μ and c refer to carrier flow rate (50 mL/min) under room temperature and detected CO volume fraction at given time *t*, respectively. V* (24.5 L/mol) stands for molar volume of ideal gas at room temperature.

Energy Consumption

$$\theta = \frac{\int_0^t UIdt}{n \cdot M} \tag{S10}$$

where θ stands for energy consumption (kWh/kg_{CO_2}) for electro-transforming 1 kg of CO_2, U (V) and I (A) refer to cell voltage and current at given time t (h) during electrolysis, respectively. n (mol) denotes to total molar amount of obtained CO_2RR products, and M (g/mol) represents molar mass of CO_2, M=44 g/mol.

Supplemental References

Deng, B., Chen, Z., Gao, M., Song, Y., Zheng, K., Tang, J., Xiao, W., Mao, X., Wang, D. (2016). Molten salt CO_2 capture and electro-transformation (MSCC-ET) into capacitive carbon at medium temperature: effect of the electrolyte composition. Faraday Discuss. 190, 241–258.

Deng, B., Mao, X., Xiao, W., Wang, D. (2017). Microbubble effect-assisted electrolytic synthesis of hollow carbon spheres from CO_2. J. Mater. Chem. A 5, 12822–12827.

Deng, B., Tang, J., Gao, M., Mao, X., Zhu, H., Xiao, W., Wang, D. (2018). Electrolytic synthesis of carbon from the captured CO_2 in molten LiCl–KCl–$CaCO_3$: Critical roles of electrode potential and temperature for hollow structure and lithium storage performance. Electrochim. Acta 259, 975–985.

Kaplan, V., Wachtel, E., Gartsman, K., Feldman, Y., Lubomirsky, I. (2010). Conversion of CO_2 to CO by electrolysis of molten lithium carbonate. J. Electrochem. Soc. 157, B552–B556.

Kikuchi, T., Ishida, R., Natsui, S., Kumagai, T., Ogino, I., Sakaguchi, N., Ueda, M., Suzuki, R.O. (2015). Carbon nanotube synthesis via the calciothermic reduction of carbon dioxide with iron additives. ECS Solid State Lett. 4, M19–M22.

Küngas, R. (2020). Review—Electrochemical CO_2 reduction for CO production: comparison of low- and high-temperature electrolysis technologies. J. Electrochem. Soc. 167, 044508.

Matsuura, F., Wakamatsu, T., Natsui, S., Kikuchi, T., Suzuki, R.O. (2015). CO gas production by molten salt electrolysis from CO_2 gas. ISIJ Int. 55, 404–408.

Yin, H., Mao, X., Tang, D., Xiao, W., Xing, L., Zhu, H., Wang, D., Sadoway, D.R. (2013). Capture and electrochemical conversion of CO_2 to value-added carbon and oxygen by molten salt electrolysis. Energy Environ. Sci. 6, 1538–1545.